USING A HYPERSPECTRAL SENSOR MOUNTED ON AN UNOCCUPIED AIRCRAFT SYSTEM TO DETECT BIOLOGICAL SOIL CRUST'S SPATIAL DISTRIBUTION IN THE CHIHUAHUAN DESERT ECOSYSTEM TO DETERMINE THEIR ANNUAL CARBON FIXATION CAPACITY

BY

Seth Burruss

A thesis submitted to the Graduate School in partial fulfillment of the requirements

for the degree

Master of Science

Major: Plant and Environmental Sciences
Minor: Geography

NEW MEXICO STATE UNIVERSITY

LAS CRUCES, NEW MEXICO

(JANURARY 2023)

Seth Burruss
Candidate
Plant and Environmental Sciences
Major
This Thesis is approved on behalf of the faculty of New Mexico State University, and it is
acceptable in quality and form for publication:
Approved by the thesis Committee:
Colby Brungard
Chairperson
Michaela Buenemann
Committee Member
Niall Hanan
Committee Member

ACKNOWLEDGEMENTS

A special thanks to my committee members at New Mexico State University Dr. Brungard, Dr. Buenemann, Dr. Hanan, and Dr. Pietrasiak for all their assistance with planning, troubleshooting, and the review process during this research project. Their input and guidance were invaluable during the ups and downs of this work. I also want to recognize and thank Mikaela Hoellrich for her sizable contribution to this project in collecting the LPI data and for sharing her BSCs carbon sequestration data. I would like to thank Dr. Santiago and Dr. Vargas from the University of Texas El Paso for lending us the drone used to collect our data and assistance in the field.

Lastly, I would like to thank the Jornada LTER for awarding me the graduate student fellowship for two summers which supported me during this project.

VITA

EDUCATION:

M.S. Degree in Plant & Environmental Science New Mexico State University, Las Cruces NM 2020-Present

B.S., Environmental Science 2009-2011

Ferrum College, Ferrum, VA

Field of Study

Plant and Environmental Sciences Major Field:

Minor: Geography

ABSTRACT

USING A HYPERSPECTRAL SENSOR MOUNTED ON AN UNOCCUPIED AIRCRAFT SYSTEM TO DETECT BIOLOGICAL SOIL CRUST'S SPATIAL DISTRIBUTION IN THE CHIHUAHUAN DESERT ECOSYSTEM TO DETERMINE THEIR ANNUAL CARBON FIXATION CAPACITY

By

Seth Burruss

Master of Science

NEW MEXICO STATE UNIVERSITY

LAS CRUCES, NEW MEXICO

January 2023

Dr. Colby Brungard

Biological soil crusts (BSCs) consist of cyanobacteria, algae, fungi, lichens, and mosses, which live within the uppermost millimeters of the soil's surface where they influence soil stability, nitrogen, and carbon cycles. BSCs are only a few millimeters thick but cover large expanses of ground allowing for possibly significant contributions to the carbon cycle in arid environments. Remote sensing of these organisms has been used to study BCS in a non-destructive manner over the last 36 years. In this project, we aimed to quantify the abundance and distribution of BSCs and to estimate their annual carbon fixation rate at different community stages in two unique research sites (T-East and T-West) in the Chihuahuan desert of southern New Mexico, USA. We first investigated the utility of an unoccupied aircraft system (UAS)-mounted hyperspectral camera to measure the spatial cover of two BSCs functional groups (light and dark BSC) in a

shrub-dominated vs. predominantly grassland site. Using a spectral angle mapper (SAM) algorithm we classified the hyperspectral imagery into five cover classes (light BSC, dark BSC, bare soil, grasses, and shrubs). With observations collected utilizing a line point intercept (LPI) method, we quantified the percent cover of BSCs and vegetation within the transects to validate the SAM estimates. Lastly, we incorporated C-fixation rates from local BSC communities to estimate the mean annual C-fixation rates for both BSCs within our research plots. The SAM algorithm overestimated light biocrust (LBC) in T-East by 17.7% when compared with the LPI estimates. Inversely, the SAM underestimated dark biocrust (DBC) for T-East by 9.3% as well as underestimating both Light and DBCs for T-west (23.9% and 6.7% respectively) when compared to the LPI estimates. This produced a higher annual fixed CO2 value for T-East's LBC of 36.4% and a lower rate for DBC of 37.2% in comparison with the LPI's observations. The T-West annual fixed CO₂ was underestimated by the SAM algorithm by 66.1% for LBC and 42.9% for DBC when compared to the LPI observations. The results indicate the heavily shrub-encroached T-East site had a better accuracy rate than the T-West grassland site for the accurate classification of the five cover classes. It was believed that the vegetation's close proximity to the soil surface and sample timing negatively interfered with the detection rates of light and dark BSCs.

Keywords: biological soil crust, remote sensing, spectral angle mapper, annual carbon fixation

TABLE OF CONTENTS

ACKNOWLEDGEMENTS	iii
VITA	iv
ABSTRACT	v
TABLE OF CONTENTS	vii
LIST OF TABLES	viii
LIST OF FIGURES	ix
INTRODUCTION	1
METHODS	6
RESULTS	17
DISCUSSION	25
CONCLUSION	33
REFERENCES	35

LIST OF TABLES

Table 1: LPI measurements and the SAM estimates. The classes represent the five ground cover classes within the NPP plots. The LPI column is the measured ground cover percentage by class. The SAM column is the estimated ground cover percentage by class. The difference column shows the difference between the LPI% and the SAM% values. Negative numbers indicate higher SAM estimates than LPI measurements by SAM and positive values are lower estimates than LPI measurements. Zero indicates no difference.

Table 2: Chi-Square goodness of fit test's p-values comparing the SAM estimates from the LPI observed values.

Table 3: Average estimates of the maximum annual carbon fixation rates for LBC and DBC (Hoellrich, 2021).

Table 4: Estimated total annual fixed grams of CO₂ m⁻² yr⁻¹ for LBC, DBC using LPI and SAM for both NPP sites.

LIST OF FIGURES

Figure 1: Diagram showing the placement of the 4 x 50 m transects within the Net Primary Productivity (NPP) T-east and T-west sites at the Jornada Experimental Range. The dashed grey line represents transect 1 and transect 2 in the NPP sites. Both the T-east and T-west NPP sites are laid out in the same fashion. Hollow circles indicate ½" rebar stakes marking the corners of the 70 m x 70 m site. Solid black circles indicate ¾" rebar stakes which lay out the interior of the NPP sites. The diagram was redrawn from Dr. Pietrasiak's Jornada notification of proposed research study # 467, (2016).

Figure 2: Diagram indicates the 50m x 4m transect with the 10m buffer. The solid light blue line marks the LPI location within the plot. Solid black circles indicate 3/8" rebar stakes which locate the interior sections in the NPP sites. The diagram was redrawn from Dr. Pietrasiak's Jornada notification of proposed research study # 467, (2016).

Figure 3. A redrawn plot of a test and reference spectra of a two-band image following Kruse et al. (1993).

Figure 4: Field reflectance scans of bare soil, grass, shrubs, DBC, and LBC from both NPP sites. In T-East (right), Bare soil has the highest reflectance values followed by LBC with the second highest overall values. Shrubs are the third highest with a pronounced peak around 780-930 nm. Grasses and DBCs have the lowest recorded reflectance values. T-West (left) scans show similar results, but shrubs have the second highest reflectance value over LBCs.

Figure 5: Bar chart of the T-East and T-West NPP sites comparing the average percent cover from both LPI and SAM methods.

Figure 6: Pseudo color composite of T-West and T-East NPP sites orthorectified hyperspectral full reflectance images. Represented by three bands located in the Red (band 110, 640.74nm), Green (band 69, 549.97nm), and Blue (band 33, 470.28nm) color spectrum.

INTRODUCTION

Over a billion people live in and depend on arid and semiarid ecosystems that are experiencing increasing water scarcity, human population growth, desertification, and land use degradation reinforced by the effects of climate change (Rodríguez -Caballero et al. 2017; Maestre et al. 2012). These are a few of the principal driving factors focusing land managers and environmental scientists to promote research that increases our understanding of our arid ecosystems. Drylands cover a vast expanse of land estimated at approximately 40% of the Earth's terrestrial surface (Masestre et al. 2012) and are believed to contain 10 x 10¹⁵ g C illustrating the need to understand the controls of carbon fluxes within these biomes (Saugier et al. 2001). These systems are not barren wastelands void of flora and fauna but are often characterized by high biodiversity, providing unique habitats for many organisms from large herbivores to complex and diverse vegetation structures, and biological soil crusts (BSC).

Biological Soil Crust is a complex community of bacteria, cyanobacteria, algae, fungi, lichens, and mosses that occur on or near the soil's surface (Belnap et al. 2016). Globally, communities of BSC are estimated to cover approximately 12% of the earth's terrestrial surface (Rodríguez -Caballero et al. 2018) and dominate 40-100% of the open grounds surface in drylands (Ferrenburg et al. 2017; Caballero et al. 2017; Belnap et al. 2016). BSCs are currently estimated to contain 56 x 10¹² g C held in cyanobacterial (light BSCs) in arid and semiarid regions (Garcia-Pichel et al. 2003). In ecosystems where water and available nutrients limit vascular plant cover (Belnap et al. 2016), BSC performs critical ecosystem services such as soil

aggregation, carbon fixation, nitrogen fixation, evaporation, water infiltration, and the air-to-soil gas exchange (Pietrasiak et al. 2013; Rodríguez -Caballero et al. 2014). These BSC communities are often distributed in a heterogenous patchwork across the landscape where their diverse community structures differ in their degree of influence on ecosystem functions (Pietrasiak et al. 2013; Belnap et al. 2016; Caballero et al. 2017). These diminutive communities are increasingly being recognized to have global-scale ecological impacts on the climate, carbon, nitrogen, and hydrological cycles (Rozenstein et al. 2017). However, accurate measurements of BSC's coverage, nitrogen fixation rates, and effects on the carbon cycle are currently limited.

The C-fixation rates of BSCs are dependent on the species type and abundance within the crust (Grote et al. 2010). It is currently believed that changes to climate and land use practices are negatively impacting BSCs by converting later succession stage crust to early successional stages leading to lowered drylands system's C-fixation rates (Housman et al. 2006). This observed trend has the potential to add up to large amounts of carbon not being sequestered from the atmosphere exacerbating the effects of climate change. To determine how the carbon cycle and BSCs may change in the future facing the increasing variable climate requires an accurate and efficient means of detecting species composition and density of BSC.

Over the last few decades, a great deal of effort has been spent identifying and mapping BSCs using traditional fieldwork density assessment methods which have proved to be costly, time-consuming, and to have difficulties determining species composition in the field (Karniel et al. 1999; Chen et al. 2005; Weber et al. 2008; Chamizo et al. 2010). The vast expanses of drylands, the high heterogeneity of BSC distribution, and their vulnerability to physical

disturbance is leading scientists to turn to remote sensing to collect data on these communities (Chamizo et al. 2010). Aerial surveys via drone or satellite imaging have shown promising results in detecting BSC's community distribution and species composition without further leading to site degradation.

The use of remote sensing techniques for mapping BSCs was first recognized by Wessels and Van Vuuren in 1986 who used satellite imagery of Landsat Thematic Mapper 3 (Bands 4, 5, 7) to identify lichen-moss dominated BSCs in the Namib Desert. Shortly after, O'Neil described the spectral characteristics of BSC's local absorption feature of chlorophyll a at (675 nm) and noted BSCs spectral response to wetting in 1994 (O'Neil et al. 1994). Since this initial application, many studies have promoted BSC identification techniques using remotely sensed data (Karnieli et al. 1999; Chen et al. 2005; Weber et al. 2008; Chamizo et al. 2010; Rodríguez et al. 2014; Rozenstein et al. 2017). BSC's communities have been distinguishable due to organic components found within the crust (phycobilin, chlorophyll, cellulose, lignin, starch, and wax) (Rozenstein et al. 2017; Rodríguez et al. 2014). The reflectance of BSC is explainable by absorption features due to (0.430 μm) phycobilin in cyanobacteria, (0.680 μm) chlorophyll, (1.720 μm) cellulose and lignin, (2.080 μm) starch, lignin, and wax, and (2.309 μm) humic acid, wax, and starch (Rozenstein et al. 2017). These components enable biocrust to be distinguishable from the heterogenous cover types prominent in dryland ecosystems. However, detection rates of BSCs using remote sensing tools are highly affected by environmental conditions (Chen, et al. 2020). When BSCs are dry they exhibit a spectral response similar to bare soil and when sufficient water is present they conduct photosynthesis and appear plant-like (Weber et al. 2008;

Rozenstein et al. 2017). The spectral signature of BSC under these wet conditions can be like that of higher plants, producing high values in the NDVI (Rozenstein et al. 2017), which has led to misinterpretation of ecosystem productivity and vegetation dynamics (Karnieli et al. 1999). Other spectral commonalities show that when dry there is an overall lower reflectance value of BSC when compared to the soil (Chen et al. 2005; Karnieli et al. 1999) suggesting that when using multispectral data during the rainy season is it important to examine the red and red edge bands region to estimate biocrust more accurately cover (Chen et al. 2020). Correctly timing sampling to early spring following the rains before annuals have germinated and the perennials are still dry (Chen et al. 2020), can lead to higher success in distinguishing BSC coverages.

Initially, remote detection of BSCs used low to moderate-resolution satellite imagery like Landsat and Moderate Resolution Imaging Spectroradiometer (MODIS) (Rodriguez et al. 2014; Weber et al. 2016). This can be problematic as BSCs generally co-occur with vegetation and can lead to mixed reflectance pixel values. Although satellite remote sensing is useful for large-scale BSCs cover assessments, newer high-resolution 3-band multispectral sensors on unmanned aerial systems (UASs) have recently been used successfully to map BSCs in Southeastern Utah at finer scales (Havrilla et al. 2020). However, multispectral sensors do not provide the same level of spectral resolution as hyperspectral sensors and only provide data in the visible region of the electromagnetic spectrum. This makes it difficult for multispectral sensors to discern the organic components and fine reflectance differences of BSCs. Hyperspectral sensors, which have hundreds of continuous bands and can examine larger areas within the electromagnetic spectrum, may currently be the best-suited method for remote detection of BSCs.

Hyperspectral and multispectral sensors have both been used to effectively map BSC distribution and to distinguish different successional stages across a heterogenous landscape (Havrilla et al. 2020; Weber et al. 2008). Using reflectance values through the visible, near-infrared (NIR), and short-wave-infrared electromagnetic ranges show good results and has led to the development of multiple classification indices including the Crust Index, Biological Soil Crust Index, Continuum Removal Crust Identification Algorithm, and Crust Development Index (Rodriguez et al. 2017).

The primary goal of this research was to quantify the abundance and distribution of biocrust at two unique research sites. These sites represented two different ecological vegetation states of shrub encroachment (high and low) in a historically warm season grassland system. We investigated the utility of a UAV-mounted hyperspectral sensor to measure the spatial cover of BSCs in a shrub-dominated vs. predominantly grassland site located in the Chihuahuan desert, Southern New Mexico. Then subsequently incorporate C-fixation rates from local BSC communities to estimate the mean annual C-fixation rates for BSCs within our research plots.

METHODS

Site description

The study area was located in the Chihuahuan desert ecosystem of southern New Mexico, USA, within the 101,000-hectare Jornada experimental range. The regional climate of the study area is semiarid with a long-term mean annual precipitation of (245.1 mm) with a standard deviation of (85.0 mm) (Havstad et al. 2006). The primary land use at the Jornada is long-term research focused on increasing the sustainability and resilience of multiple land use techniques in modern-day semi-arid rangelands. This includes livestock production, ecological restoration, vegetation monitoring, and managing ecosystem change. This study focused on two sites that are part of Jornada's Net Primary Productivity (NPP) plots. Both sites are approximately 1315 m above sea level. These sites represent undisturbed (*ungrazed*) ecosystems and were selected for their quality BSC communities.

To explore BSC community differences relating to vegetation structure and ecological state change, two locations representing different points of grassland-to-shrubland transition were selected for comparison. Site 1, hereafter called T-east, is a shrub encroached historical grassland site dominated by *Flourensia cernua DC*. (Tarbush), *Muhlenbergia Porteri Scribn* (Bush muhly), *Bouteloua eriopoda Torr*. (Black grama), and *Scleropogon brevifolius Phil*. (Burro grass). The soil surface is a fine sandy loam (SoilWeb 2022). Site 2, hereafter called T-west is a minimally shrub encroached historical grassland site dominated by *Flourensia cernua DC*. (Tarbush), and *Scleropogon brevifolius Phil*. (Burro grass). The soil surface is a fine sandy

loam. (SoilWeb 2022). Vegetation identification came from historical site data provided by the Jornada.

The T-East and T-West NPP sites are located on the boundary of a historical grassland ecosystem being encroached by shrubs from the East. T-East has notably higher shrubs and fewer graminoids than T-West. This successional process is referred to as an ecological state transition and can be seen in Figure 6. This provided a unique opportunity to measure the different vegetative state's effects on remote sensing detection rates of the NPP site's BSCs communities.

Transect data collection

In February 2022 we established four (two in each of the NPP sites) 50 m transects, with a 10m buffer to avoid edge effects (These are referred to as transect 1 and transect 2 respectively) within each of the T-west and T-east sites. Figure 1 indicates the location of the transects within the study sites. A detailed schematic of the transect design is shown in Figure 2. The line point intercept (LPI) method was employed to quantify the percent cover of BSCs and vegetation within the transects (Herrick et al. 2018). To create the transects, a measuring tape was stretched the length of the 50 m transect and a pin flag was dropped every 0.25 m. The ground cover was recorded as 1 of 5 cover classes at each pin-flag fall (bare soil, shrubs, grasses, dark biocrust (DBC), and light biocrust (LBC). This resulted in 200 observations of ground cover along each transect. Following field observation, the cover classes were converted to the percentage of ground cover for each transect (Herrick et al. 2018).

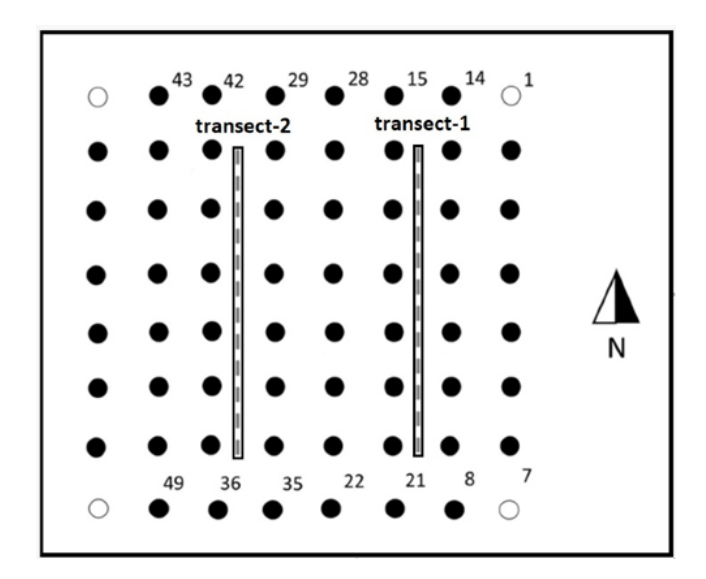


Figure 1: Diagram showing the placement of the 4, 50 m transects within the Net Primary Productivity (NPP) sites at the Jornada Experimental Range. The dashed grey line represents transect 1 and transect 2 in the NPP sites. Both the T-east and T-west NPP sites are laid out in the same fashion. Hollow circles indicate ½" rebar stakes marking the corners of the 70 m x 70 m site. Solid black circles indicate ¾" rebar stakes which lay out the interior of the NPP sites.

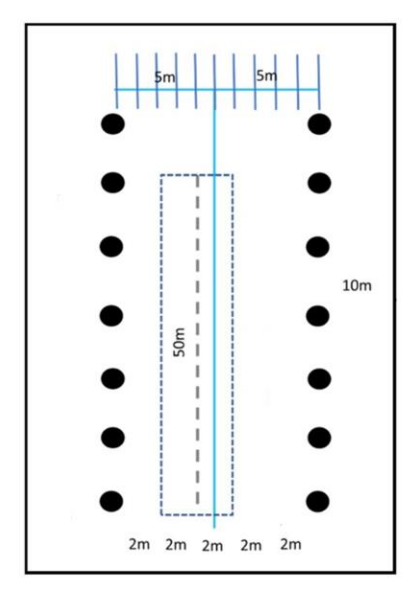


Figure 2: Diagram indicates the 50m x 4m transect with the 10m buffer. The solid light blue line marks the LPI location within the plot. Solid black circles indicate 3/8" rebar stakes which locate the interior sections in the NPP sites. The diagram was redrawn from Dr. Pietrasiak's Jornada notification of proposed research study # 467, (2016).

In-field spectral reflectance measurement

The spectral signatures of DBC, LBC, bare soil, grasses, and shrubs were measured using an Analytical Spectral Devices (ASD) FieldSpec-IV spectroradiometer backpack scanner during UAS hyperspectral collection. The FieldSpec-IV measured reflectance between 350-2500 nm. The device's spectral sampling bandwidth was 1.4 nm between 350-1000 nm and 1.2 nm between 1001-2500 nm. The sensor was fitted with a 3° field of view (FOV) attachment. The senor was held approximately 20 cm above the sample for the soil surface scans (bare soil, DBC,

LBC) (area scanned 1.05 cm²), and 50 cm for the vegetation scans (shrubs, grasses) (area scanned 2.62 cm²) at nadir to ensure a consistent sampling technique for each sample class. Bare soil scans were taken from the pathway leading into the NPP sites. LBC scans were identified due to the darkened greenish hue prominent in the sites after the recent rains. Small soil plugs were excavated and examined to verify whether a developed crust was present or absent prior to sampling. The measurements were taken with clear sunny conditions between 12:54-1:12 pm for T-east plots, and 1:24-1:42 pm for T-west transects MST. Each scan was taken as an average of 25 individual scans, and the samples were collected in reflectance format. Twenty sample scans were collected for the dark biocrust, light biocrust, and grasses while ten sample scans were collected for the shrub and bare soil for a total of 70 sample scans. The FieldSpec-IV was calibrated using a white reference panel every five samples to account for atmospheric change. This sampling design was chosen due to the highly heterogeneous nature of BSC's composition (Pichel et al. 2016).

Unmanned Aerial system data collection

A two-hundred and seventy band hyperspectral image was collected on October 11, 2022 for both transects at both sites using a Headwall Nano hyperspectral sensor (12 mm lens) mounted on DJI Matrice 600 Pro hexacopter with a Ronin-MX Gimbal kit. The Headwall nano sensor collected 270 spectral bands in the VNIR range (400-1000 nm) of the electromagnetic spectrum at a frame rate of 300 Hz. The spectral band sampling width was 2.2 nm between 400-1000 nm. Prior to the flights, we located the ends of the flight lines by measuring out 6 m east of

the rebar stakes (numbers 15, 21, 36, 42 in Fig. 1). Temporary pin flags were placed at these points and the GPS coordinates were recorded. These GPS coordinates were used in the UgCS mission control flight planning software to guide the UAV along the transect path. Additionally, during this time white reference panels were placed at both ends of the transect in line with the pin flags, and ground targets were located around the transects rebar stakes on the Western edge of the transect. The soil surface conditions during this time were damp due to a light rain shower during the night or from heavy dew. Reliable precipitation measurements were not available for this period of time.

Immediately before data collection the Headwall Nano hyperspectral camera was calibrated using a Spectralon® Diffuse Reflectance panel. This was done to ensure consistent reflectance values between sampling events. The flights were conducted between 10:28 am MST for the T-east site, and the last flight concluded at 12:13 pm MST for T-west. The average sustained altitude during the flight was 30 m. The wind speed during the flight times was low; approximately 0.45-2.24 ms⁻¹ at the ground surface. Cloud conditions were clear during the flights.

After the aerial images were collected and downloaded using Headwalls Hyperspec®III software. We performed two pre-processing steps with the hyperspectral data. First, the gps.imu data file that was recorded with the imagery was corrected using Trimble Applanix Postpac UAV software. This corrected the GPS flight points by offsetting them using nearby permanent base stations. Lastly, the aerial imagery was orthorectified using Headwalls SpectralView® software.

The orthorectification process stretched the hyperspectral image over a digital elevation model (DEM) accounting for the topographic variability within the site. The DEM had a 1m resolution and was acquired using the U.S. Geological Survey's EarthExplorer web application (USGS EarthExplorer, 2022). The mosaicked hyperspectral aerial image's resolution (ground sampling distance) was approximately 1.84 cm per pixel.

Image classification

Spectral Angle mapper (SAM) was used to classify pixels into one of five cover classes using the aerial hyperspectral imagery and the FieldSpec-IV field scans. SAM is a supervised spectral classification model that uses a multidimensional angle to match imagery spectra to reference spectra (Kruse et al. 1993). The algorithm determines the spectral similarity between the reference spectra and image spectra by treating them as vectors in space with dimensionality equal to the number of bands (Petropoulos et al. 2010). SAM compares the angle between the reflectance spectra kernels (FieldSpec-IV .asd scans) to each pixel within each band simultaneously. The smaller the angle between the spectra the closer the match. Pixels greater than a specified maxim angle threshold would not be classified (Kruse et al. 1993) (Figure 3). This study used 0.10 rad as the threshold. The SAM classification assumes that the data is in reflectance format and is relatively insensitive to illumination and albedo effects (Shafri et al. 2007). This, paired with the SAM's ability to rapidly map spectral similarities between image spectra and reference data in hyperspectral images, makes it a valuable tool for hyperspectral image classification.

The SAM supervised classification process was implemented as follows. In the Environment of Visualizing Images (ENVI) software version 5.6 (64-bit), we imported the aerial hyperspectral imagery for the four transects. Using the quick statistics tool located in the data manager. We examined the histogram of all 270 bands' digital reflectance numbers to determine where to trim the beginning and end bands that contained the highest variability. Spectral trimming is a preprocessing tool aiming to improve the spectra's quality by removing some of the bands before using them for qualitative analysis. It is a common step in preprocessing hyperspectral images to remove wavelength ranges with high signal-to-noise ratios (Wadoux et al. 2021). To remove the bands, we used the spectral subset option found in the Spectral Angle Mapper (SAM) tool to keep the region between 479.1370 - 919.684 nm for classification. The next step was to create a region of interest (ROI) using the ROI polygon tool and the ruler function to pull measurements off the ground targets located around the rebar markers to select only the transect area for classification. The ROI was selected using the spatial subset option found under the SAM classification tool parameters.

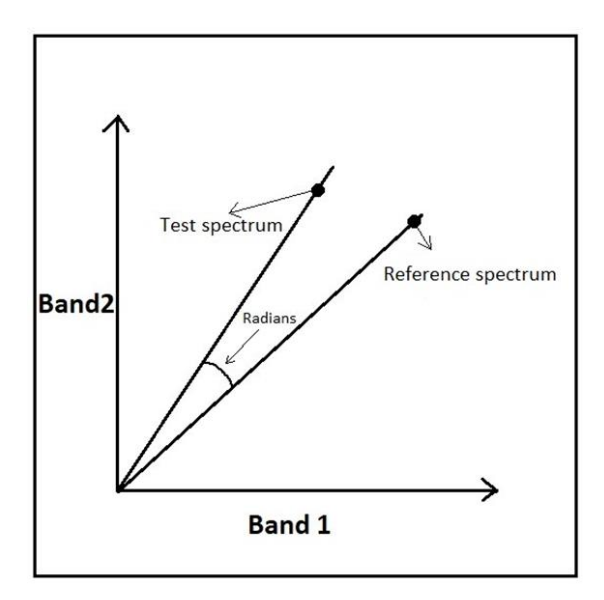


Figure 3. A redrawn plot of a test and reference spectra of a two-band image following Kruse et al. (1993).

Method Comparison

A comparative analysis was used to examine the correlation of the 5 ground cover class percentages between the LPI transect measurements and the SAM classification. To do this we compared the difference in ground cover estimates (LPI observations and SAM's estimations) to assess the classification accuracy. This methodology was chosen as a more traditional ground truthing process was not permitted inside the long-term NPP sites which have strict access restrictions to protect the 33 year old study sites.

A Chi-Square test of independence was used to determine if the SAM cover estimates and LPI cover measurements were independent of one another. If the results show the cover

estimates are not independent from one another one could conclude the LPI observations matched the SAMs estimates with a 95% probability. A Chi-Square goodness-of-fit test was performed by transect to test whether the SAM cover estimates matched the observed probability from the LPI measurements. Lastly, a nonparametric Wilcoxon signed-ranked pairs analysis was used to determine the difference between the matched pairs between the SAM estimates and LPI measurements. The Wilcoxon p-value indicates the probability that the null hypothesis is true and that both populations are the same. The closer the value is to 1 the more likely the matched pairs of the five ground cover classes are not significantly different. Inversely the closer to zero the p-value is the less probable the 5 matched pairs are from the same population and are different. All statistical analyses were performed using RStudio version 4. 2. 0. (2022-04-22 ucrt) and statistical significance was set to 0.05.

Carbon Fixation

Biocrust sampling for carbon fixation rates was conducted from May through July 2020 approximately 500 m Southeast of the NPP plots by Mikaela Hoellrich. Two 30m transects were established forming an "X" at 15 m. Along these transects, 25 samples for each of the five BSCs types were collected (light cyanobacteria/algal, dark cyanobacteria/algal, phycolichen *Clavascidium*, cyanolichen *Peltula*, and moss biocrust) (Hoellrich, 2021). A total of 125 samples were collected from the site (5 samples from each of the five BSCs types and x5 for replications). The maximum annual average carbon fixation results of 5 BSC classes were combined into the two functional groups light (LBC) and dark (DBC) cover classes to match the

aerial survey (Table 3). The LBCs class represented the light cyanobacteria/algal BSCs. The DBCs class included the dark cyanobacteria/algal, phycolichen *Clavascidium*, cyanolichen *Peltula*, and moss BSCs groups.

CO₂ exchange measurements were made using portable photosynthesis instruments in the laboratory. This was done by cutting the BSCs with a 1.6 x 1.7 cm cookie cutter and wetting the BSCs to field capacity using distilled water. Then the BSCs were placed under low light conditions for 5 different light incubation time intervals (30 mins, 2 hrs, 6 hrs, 12 hrs, and 24 hrs). Afterwards, the BSCs were placed into the LI-COR chamber where carbon fixation measurements were recorded under ambient temperature conditions for the 5 light periods. To account for BSCs carbon fixation diversity among the different species only the highest average fixation rates recorded from the five replicates light periods were compared. Average maximum yearly carbon fixation estimation rates were then calculated for each BSC type (Equation 1). This was done using 45 days of mean precipitation > 0.01 inches recorded in El Paso, TX (NOAA, 2019) to account for the potential window for BSC activity in the field. It's well known that biocrust is only active during times when water is available and needs to be considered when determining annual rates of carbon fixation (Weber et al. 2008). For a detailed description of the methodology refer to Hoellrich (2021).

The annual rate of C-fixation rate for maximum net fixation was calculated using the modified equation from (Hoellrich, 2021):

Equation 1:
$$ACFr_{BSC} = F_{BSC} * t * r * n$$

Where F_{BSC} represents the maximum carbon fixation rates (µmol CO₂ m⁻² s⁻¹) for light or dark BSC, t equals the annual total seconds per year for 12 hours of sunlight a day (43,200 seconds), r represents the number of days experiencing greater than 0.254mm of rainfall (45 days), n represents the conversion from grams of CO₂ to µmol of carbon (1 mol CO²/1x10⁶ µmol CO²)*(1 mol CO₂)*(12 g/1 mol C)

The total maximum annual carbon fixation rates for each of the transects in the NPP sites were estimated using Equation 2.

Equation 2: total grams of
$$CO_2 m^{-2} yr^{-1} = ACFr_{BSC} * p$$

Where $ACFr_{BSC}$ represents annual carbon fixation rates for LBC or DBC and p represents the proportion of ground coverage as measured from LPI or estimated from hyperspectral imagery.

RESULTS

LPI transects

LPI transect measurements are presented in Table 1. LBCs were the most abundant cover type across both NPP sites with an average cover of 42.1%. LBC's average cover estimates were higher in T-East than T-West (48.2% and 36.1% respectively). The overall difference in light BSCs cover estimates was similar between the NPP sites (12.1%) and within the NPP sites where

the transects average difference was 12.4% (8.8% for T-East and 16.0% for T-West). DBC average coverage was 20.5% for both NPP sites but was more abundant in T-East than T-West (25.0% and 15.9% respectively). Within each NPP site, DBC cover differed between transects by 2.1% and 0.3% for T-East and T-West respectively which was substantially smaller than the difference between NPP sites (9.2%)

LPI measured average bare soil cover was 9.9% for T-East (within site difference = 3.9%) and 23.8% for T-West (within site difference = 5.9%). Measured grass cover was 11.8% for T-East (within site difference = 11.0%) and 23.6% for T-West (within site difference = 9.3%) and average shrub cover was measured to be 5.1% for T-East (within site difference = 3.9%) and 0.6% for T-West (within site difference = 0.4%).

Table 1: LPI measurements and the SAM estimates. The classes represent the five ground cover classes within the NPP plots. The LPI column is the measured ground cover percentage by class. The SAM column is the estimated ground cover percentage by class. The difference column shows the difference between the LPI% and the SAM% values. Negative numbers indicate higher SAM estimates than LPI measurements by SAM and positive values are lower estimates than LPI measurements. Zero indicates no difference.

Site:	Transects	Classes	LPI %	SAM %	Difference
T-East	1	Bare Soil	11.81	2.98	8.83
		Grasses	17.36	13.64	3.99
		Shrub	3.12	0.93	2.19
		Light BSC	43.75	65.29	-21.54
		Dark BSC	23.96	17.15	6.81
	2	Bare Soil	7.91	2.75	5.16
		Grasses	6.32	15.34	-9.02
		Shrub	7.11	1.23	5.88
		Light BSC	52.57	66.39	-13.82
		Dark BSC	26.09	14.29	11.8
T-West	1	Bare Soil	26.77	15.44	11.33
		Grasses	28.35	51.94	-23.59
		Shrub	0.79	4.07	-3.28
		Light BSC	28.08	16.43	11.65
		Dark BSC	16.01	12.11	3.9
	2	Bare Soil	20.90	30.63	-9.73
		Grasses	18.97	53.83	-34.86
		Shrub	0.32	1.50	-1.18
		Light BSC	44.05	8.02	36.03
		Dark BSC	15.75	6.02	9.73

Field Reflectance Spectra

Reflectance spectra of BSC, bare soil, and vegetation showed differences in overall reflectance values and in unique spectral features but showed little difference between the two NPP study sites (Figure 4). All the cover classes range between 15% - 40% reflectance. LBC spectra exhibited higher reflectance than DBC, but bare soil had the highest overall reflectance values.

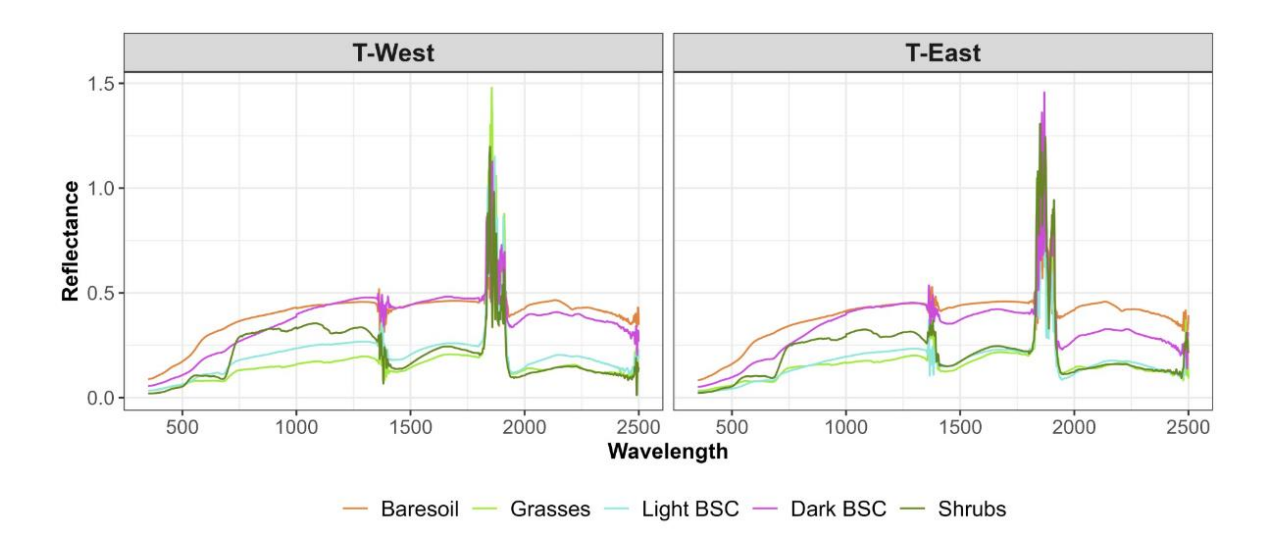


Figure 4: Field reflectance scans of bare soil, grass, shrubs, DBC, and LBC from both NPP sites. In T-East (right), Bare soil has the highest reflectance values followed by LBC with the second highest overall values. Shrubs are the third highest with a pronounced peak around 780-930 nm. Grasses and DBCs have the lowest recorded reflectance values. T-West (left) scans show similar results, but shrubs have the second highest reflectance value over LBCs.

SAM estimates

SAM cover estimates are presented in Table 1. LBC cover was among the most abundant cover types on both NPP sites with a total average LBC cover of 39.0% for both sites. The estimated average LBC cover was highest for T-East at 65.8% (within site difference of 1.1%) and 12.2% for T-West (within site difference of 8.4%). Average LBC cover varied more between NPP sites (53.6% difference) when compared to within site differences (1.1% for T-East and 8.4% for T-West). The estimated average DBC cover was higher for T-East at 15.7% (within site

difference of 2.9%) than the 9.1% cover estimate for T-West (within site difference of 6.09%). Average DBC cover varied more between NPP sites (6.6% difference) when compared to transects within a site where differences again are smaller and ranged from 2.9% and 6.09% (for T-East and T-West respectively).

Average estimated bare soil cover was higher at T-West at 23.0% (within site difference of 15.5%) than the 2.9% cover estimates for T-East (within site difference of 0.23%). The estimated average shrub cover was higher for T-West at 2.8% (within site difference of 2.6%) than the 1.1% estimate for T-East (within site difference of 0.3%). The estimated average grass cover was higher for T-West at 52.9% (within site difference of 1.9%) than the 14.4% for T-East (within site difference of 1.7%). Grasses had the highest predicted cover class area for T-West followed by bare soil and LBC.

LPI & SAM comparison

Both LPI measurements and SAM estimates demonstrated that LBC was one of the most abundant cover classes (Figure 5). The average LPI measured LBC cover was 42.1% and the average SAM estimates were 39.0%. The LPI observed average LBC was highest for T-East at 48.16% and 36.1% for T-West compared with the estimated SAM average LBC for T-East at 65.84% and 12.2% for T-West (difference of 17.7% for T-east and 23.9% for T-West).

The average DBC was lower than LBC across both sites with the total average LPI observed equaling 20.5% and the total average SAM estimated equaling 12.4%. The LPI observed average DBC was highest for T-East at 25.0% and 15.9% for T-West compared with

the estimated SAM average DBC for T-East at 15.7% and 9.1% for T-West (difference of 9.3% for T-east and 6.8% for T-West).

The LPI observed average bare soil was lower for T-East at 9.9% and 23.8% for T-West compared with the estimated SAM average bare soil for T-East at 2.9% and 23.0% for T-West (difference of 7.0% for T-east and 0.8% for T-West). The LPI observed average grasses were lower for T-East at 11.8% and 23.7% for T-West compared with the estimated SAM average grasses for T-East at 14.5% and 52.9% for T-West (difference of 2.7% for T-east and 29.2% for T-West). The LPI observed average shrub was highest for T-East at 5.1% and 0.6% for T-West compared with the estimated SAM average shrub for T-East at 1.1% and 2.8% for T-West (difference of 4.0% for T-east and 2.2% for T-West).

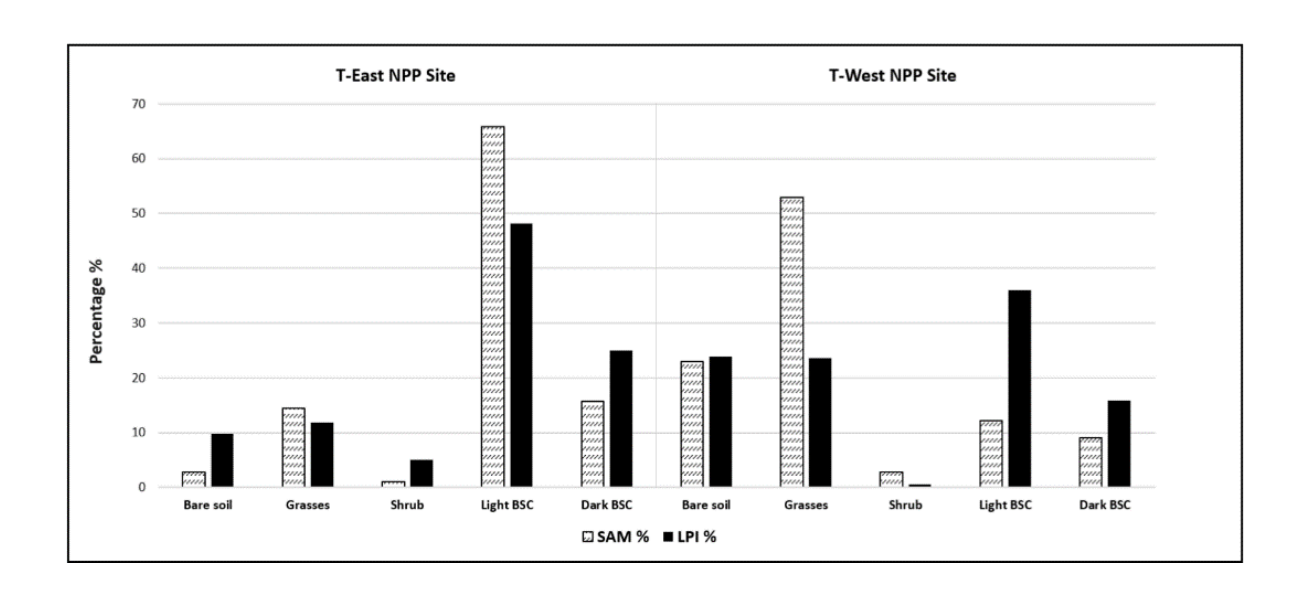


Figure 5: Bar chart of the T-East and T-West NPP sites comparing the average percent cover from both LPI and SAM methods.

The Chi-Square test for independence p-value was 0.2202 which suggests there is not enough evidence to conclude that LPI measurement and SAM estimates are independent or significantly different from one another. The Chi-Square goodness of fit results show the SAM estimates do not occur at the probabilities expected from the LPI measurements (Table 2), all results are <0.001).

Table 2: Chi-Square goodness of fit test's p-values comparing the SAM estimates from the LPI observed values.

Site:	Transect	p-value
T-East	1	2.544x10 ⁻⁰⁴
	2	4.731x10 ⁻⁰⁶
T-West	1	6.957x10 ⁻⁰⁹
	2	2.200x10 ⁻¹⁶

The nonparametric Wilcoxon signed-ranked pairs analysis for all the matched cover class pairs between the LPI measurements and the SAM estimates for T-West had a p-value of 0.7987, V = 30.5. T-East's matched pairs signed-ranked pairs had a p-value of 0.9188, V = 29.

Carbon fixation measurements

The maximum average fixation rate for BSC was $4.56~\mu mol~CO_2~m^{-2}~s^{-1}$ for LBC and $5.21~\mu mol~CO_2~m^{-2}~s^{-1}$ for DBC (Hoellrich, 2021). The annual LPI measured total fixed CO₂ or LBCs ranged from $7,672.45~g~CO_2~yr^{-1}$ to $10,264.69~g~CO_2~yr^{-1}$ depending on the site. The difference between sites was $2,592.24~g~CO_2~yr^{-1}$. In comparison, the SAMs estimated range of carbon fixation was between $2,600.73~g~CO_2~yr^{-1}$ and $14,006.79~g~CO_2~yr^{-1}$ between sites. The difference between sites was $11,406.06~g~CO_2~yr^{-1}$. The annual total fixed grams of $CO_2~for$ DBCs using the LPI observed coverage values ranged from $3,860.05~and~6,083.06~g~CO_2~yr^{-1}$ with a difference of $2,223.01~g~CO_2~yr^{-1}$. In comparison the SAM's estimated range was $2,203.51~and~3,821.21~g~CO_2~yr^{-1}$ with a difference of $1,617.70~g~CO_2~yr^{-1}$.

Table 3: Average estimates of the maximum annual carbon fixation rates for LBC and DBC (Hoellrich, 2021).

BSC Type	Fixed μmol CO ₂ m ⁻² s ⁻¹
Light BSCs	4.56
Dark BSCs	5.21

Table 4: Estimated total annual fixed grams of CO₂ yr⁻¹ for LBC, and DBC using LPI and SAM for both NPP sites.

Site:	BSC Type	LPI-Fixed grams of CO ₂ yr ⁻¹	SAM: Fixed grams of CO ₂ yr ⁻¹
T-East	Light	10,264.69	14,006.79
	Dark	6,083.06	3,821.21
T-West	Light	7,672.45	2,600.73
	Dark	3,860.05	2,203.51

DISCUSSION

We found that Hyperspectrally-derived DBC cover was always less than the LPI measurements. This is likely because the DBC at the NPP sites were found to co-occur in close proximity to shrubs which obscured the aerial sensor's view of DBCs. These patches of dark BSCs were observed during fieldwork and the pattern of their preference to occur under the northeastern sides of the shrubs was noted. This pattern can be viewed in aerial imagery for T-East (Figure 6). Physical and biological benefits of the relationship between shrubs and DBCs can include lower temperatures during times of extreme heat, protection from physical disturbances, higher amount of available nutrients, and longer access to water during rain events (Weber et al. 2008). This proximal relationship between the dark BSCs and the shrubs made it more difficult to discern BSCs from vegetation cover using the UAV hyperspectral sensor.

The relationship between the LBCs and the shrubs was opposite the DBCs. The LBCs were more prominently observed in the interspaces between the vegetation while performing the LPI. This caused SAM to estimate a higher average LBC ground cover in the T-East NPP site.

The T-East site contained large interspatial gaps between the vegetation prompting higher estimated LBCs cover when compared with the observed LBCs. Inversely T-West's light BSC coverage values had the lowest detection rate due to the high density of grasses and shrub vegetation cover.

The grass cover class was estimated higher by SAM in almost every transect except for T-East transect 1. Conversely, the shrub's SAM estimated cover values were underestimated in both NPP sites. This could have been the result of setting our SAM thresholds to favor the BSC detection over vegetation cover. It would be beneficial to be able to detect BSC and vegetation cover types equally to determine how much the vegetative community affects BSC detection. Accurate detection of all the cover types would be needed to determine if historical grasslands to shrubland state transitions alter BSC communities. This would allow for inferences to be made about the influence of climate change on BSC communities while determining the effects of shrub encroachment.

The Wilcoxon sign ranked pairs test indicated the SAM estimates were more accurate for T-East than for T-West. These results seem to correlate with the vegetation field conditions previously mentioned above. The T-West NPP site's vegetation was denser and obscured more of the soil's surface. In contrast, the vegetation at T-East had higher shrub densities, but lower grass coverage which resulted in more of the soil's surface area being detectable from the aerial sensor.

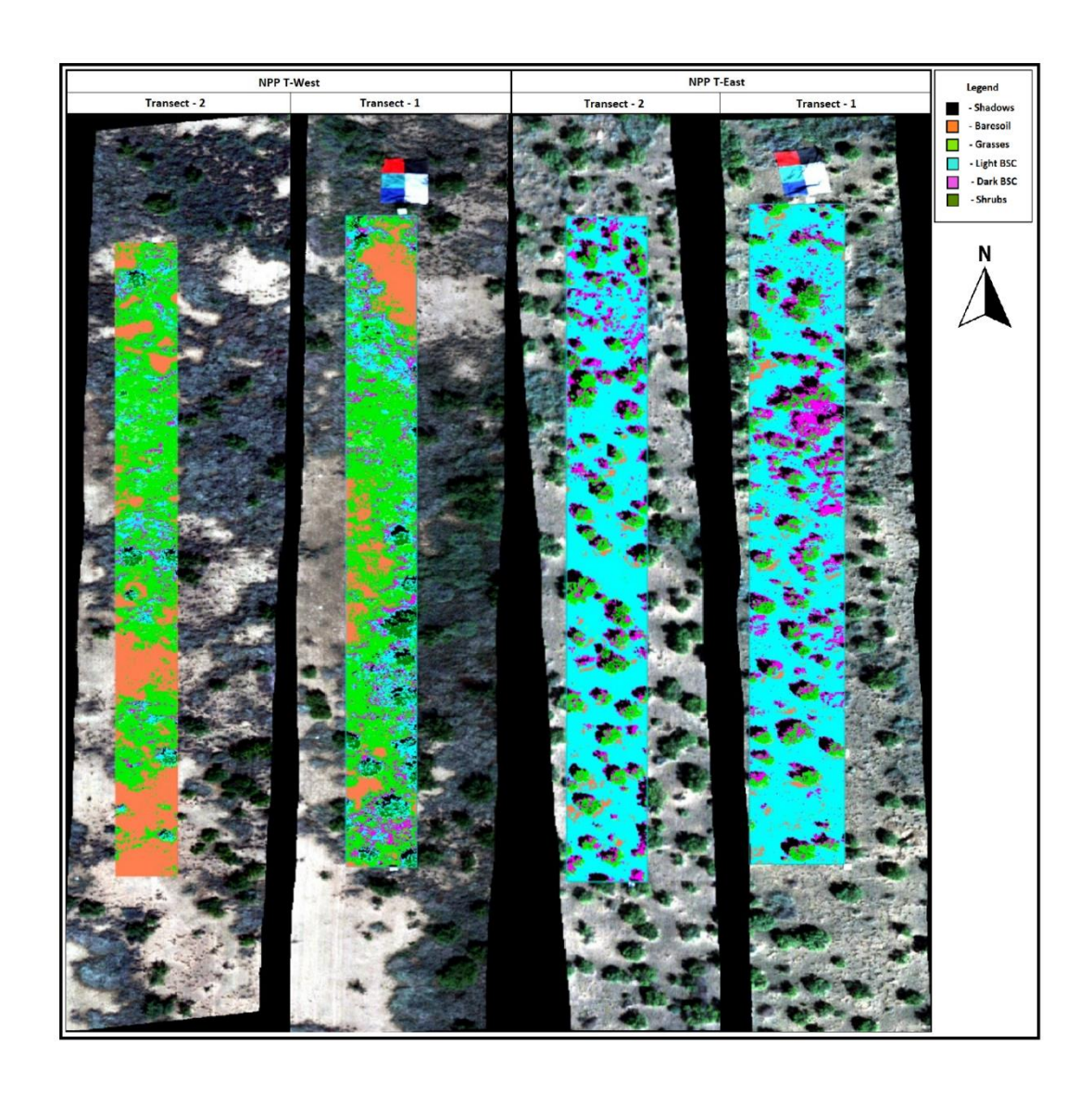


Figure 6: Pseudo color composite of T-West and T-East NPP sites orthorectified hyperspectral full reflectance images. Represented by three bands located in the Red (band 110, 640.74nm), Green (band 69, 549.97nm), and Blue (band 33, 470.28nm) color spectrum.

BSC's Carbon fixation capacity

The average estimates of the annual carbon fixation rates for light BSCs were 4.56 µmol CO₂ m⁻² s⁻¹ and 5.21 μmol CO₂ m⁻² s⁻¹ for the dark BSCs (Hoellrich, 2021). These two fixation rates appear to be closer in magnitude than the existing but limited BSC fixation rates from the Chihuahuan Desert system (Grote et al. 2010; Housman et al. 2006), who reported C-fixation rates of 1.93 µmol CO₂ m⁻² s⁻¹ in LBC and 3.49 µmol CO₂ m⁻² s⁻¹ in DBC under ideal moisture and temperature conditions (Grote et al. 2010). The estimated C-fixation rates from Hoellrich (2021) are both higher than Grote's (2010) findings and could be the result of different laboratory methodologies. It's generally believed that rates of C fixation by light BSCs are generally low (approximately 1 µmol CO₂ m⁻² s⁻¹ m2 s1), due to their lower overall biomass and chlorophyll content (Garcia-Pichel and Belnap, 1996), and is limited by lower amounts of light penetrating the sub-soils surface region which they occupy (Lange, 2003). Contrarily, dark BSCs contain lichens and mosses with greater biomass and reside on the soil surface allowing for photosynthetic rates greater than 10 µmol CO₂ m⁻² s⁻¹ (Lange, 2003; Housman et al. 2006). It is well established that the rates of carbon fixation in the same biocrust type can vary largely across different ecosystems and are often highly localized (Grote et al., 2010; Pietrasiak, 2012; Miralles et al. 2018) The rates are dependent on several abiotic factors like water and temperature which are highly variable between deserts (Grote et al. 2010).

Because the LBC SAM area estimates were higher than the LPI measurements for T-East, the total annual LBC carbon fixation rates were 36.4% higher than when using area derived from the LPI measurements. Comparatively, the DBC fixation rates from SAM were 37.2% lower than LPI for T-East. Both LBC and DBC for the T-west site were lower (66.1% and 42.9% respectively) when compared to carbon fixation rates using the LPI methodology.

Measurement Uncertainty

The cover estimates and C fixation rates suggest that substantial differences exist between ground (LPI) and aerial (SAM) measurement methodologies for detecting BSC in drylands. In addition to the physiological attributes of BSC (e.g., DBC occurring under shrubs), these differences can be partially explained by measurement uncertainties which confound definitive comparisons between methods. While it was difficult to calculate quantitative uncertainty, the following sections discuss possible, and likely common, sources of measurement uncertainty when using hyperspectral imagery to measure BSC cover. The most common sources of uncertainty occur from temporal conditions, biological behavior of biocrust, operator error and variable weather conditions.

Temporal conditions

Seasonality strongly influences the ability to remotely detect BSC. This includes the vegetative community and the BSC communities themselves. The structure of vegetation communities can change seasonally in drylands significantly. The ground surface is most visible when higher-order plants are senesced during the winter months, early spring, or before the arrival of the monsoon rains. However, during this time bare soil, dry BSCs, and vegetation can

exhibit similar spectral characteristics (Karnieli et al. 1999). The most favorable temporal conditions for detecting BSC are following the first rain event after enough time has passed to enable BSCs to become active but, before the leafing and growth of trees, shrubs, perennials, or annuals (Weber et al. 2008). This can be challenging because drylands are known to have irregular growing seasons due to unpredictable rainfall patterns and frequent periods of drought (Smith et al. 2019). Some of our measurement uncertainty may be because our field sampling and image acquisition occurred during the Fall of 2022, due to equipment problems, after the shrubs and grasses had leafed out following the summer monsoons.

Biological behavior of biocrust

Another source of difficulties encountered in remotely sensing BSC is their biological behavior. BSC's are often referred to as cryptograms because they withdraw into the soil when conditions become too dry. This effectively hides the BSC under the soil and makes it very difficult to determine their spatial coverage and community structure. This is often why LBC reflectance values will resemble bare soil (Chen et al. 2005; Karnieli et al. 1999). This can potentially be mitigated by timing image acquisition immediately following precipitation events. Additionally, as discussed above DBC tends to prefer to grow in close proximity to shrubs. This is a principal concern when measuring BSC in drylands dominated by shrubs (Havrilla et al. 2020). It can be challenging to account for BSCs growing under the shrub's canopy cover when using passive sensors. It is difficult to see how passive remote sensing could overcome this limitation.

Operator error

A common example of operator error is the wearing of different colored clothes during different field spectra measurement campaigns. Surprisingly, bright and dark clothing can influence the reflectance values of the objects of interest (Havrilla, et al. 2020), or result in inconsistent field calibration of the sensor system before data collection. Additionally, spectral measurements from different vertical angles or cardinal directions can also result in increased reflectance variability. This can lower the quality of the training data and reduce the overall effectiveness of the post-classification process. Generally, this source of uncertainty can often be minimized if the operator of the spectral measurement device (e.g., field spec) ensures that the FOV attachment is consistent during measurement.

Variable weather conditions

As previously mentioned, the timing of sampling is critical to the successful mapping of biocrust. Ideal sampling conditions include clear skies, sunny weather settings, and low wind speeds (Rodriguez et al. 2014; Karnieli et al. 1999; Havrilla et al. 2020; Weber et al. 2008; Chen et a. 2005). When using passive sensors, it is best to sample during low wind and clear atmospheric conditions. Examples of poor atmospheric conditions can include high amounts of suspended particulates like smoke, dust, and water (*humidity*). High concentrations of these in the atmosphere are known to interfere with the transmission of energy. Cloud cover can lead to changes in reflectance values and cause problems during calibration techniques. Unfortunately, it is sometimes difficult to time image acquisition for both optimal biological behavior (after a rain

event) and optimal weather conditions which can be windy and cloudy up to several days after a rain event.

Future research:

Advancements in remote sensing technology paired with reduction of cost are making it easier for scientists to collect data on the environment. Examples like Havrilla et al. (2020) which used a consumer-grade multispectral camera to map biocrust show that successful remote sensing of BSCs can be performed at a low cost. Hyperspectral sensors have also notably dropped in cost substantially over the last decade, with major improvements made to the sensors, GPS, UAV's, collection software, and processing software. However, there are still many improvements necessary before UAV-mounted hyperspectral sensor systems and software packages are off-the-shelf ready for BSC detection. One highly anticipated improvement would be the hyperspectral imagery post-processing step. Hyperspectral image analysis is currently limited to a few software programs which are expensive and have limited manipulation tools. Lastly, with advances in technology and lower costs of equipment. Thermal infrared (TIR) and high-resolution LIDAR are being incorporated into the remote detection of BSCs. TIR sensors can penetrate cloud cover, collect data within shadows, and can even be used to collect data at night (Rozenstein et al. 2017). These sensor systems could be paired with multispectral or hyperspectral sensors which could aid in BSC coverage detection under low height shrubland ecosystems.

CONCLUSION

This research investigated the utility of a UAV-mounted hyperspectral sensor to measure the spatial cover of BSCs in shrub-dominated and predominantly grassland sites and compared results to ground-based measurements. Subsequently, this research used cover estimates and C-fixation rates from local BSC communities to estimate the mean annual C-fixation rates for light (LBC) and dark (DBC) BSCs within the two research plots.

Results indicate large differences between ground-based and hyperspectral-based estimates of BSC cover. Hyperspectral imagery classification tends to estimate greater LBC and lower DBC cover than ground-based measurement. These differences translated into large differences in estimated carbon fixation rates. These differences appear to be mostly attributable to hyperspectral measurement uncertainties because of vegetation structure and the biological behavior of BSC as well as image acquisition timing. DBC were predominantly located under shrubs which made remote detection of DBC difficult in the shrub dominated plot. While LBCs were located in shrub interspaces, and hence were more easily detectable in the shrub site, the denser grass cover in the grassland site made the detection of LBCs more difficult. It is possible that the complications of vegetation structure and BSC behavior on hyperspectral BSC detection could have been mitigated had hyperspectral imagery been collected during optimal conditions. Optimal conditions for BSC detection occur shortly after the first rain event following a prolonged dry period when BSCs have become active but before the rapid growth of shrubs and grasses obscures BSC.

While UAV platforms are an attractive tool for determining the spatial distribution of BSC because they can cover large areas without causing physical degradation to BSC communities, this investigation suggests that UAV-based hyperspectral detection of biocrusts in arid rangelands may not be as accurate as ground-based measurements.

REFERENCES

Belnap, Weber, Budel, Biological soil crusts: An organizing principle in drylands. (2016). *Ecological Studies*. https://doi.org/10.1007

Burgheimer J., B. Wilske, K. Maseyk, A. Karnieli, E. Zaady, D. Yakir, J. Kesselmeier 2006. Ground and space spectral measurements for assessing the semi-arid ecosystem phenology related to CO2 fluxes of biological soil crusts. *Remote Sensing of Environment* 101:1–12.

Chamizo, S., A. Stevens, Y. Cantón, I. Miralles, F. Domingo, and B. Van Wesemael. 2012. Discriminating soil crust type, development stage and degree of disturbance in semiarid environments from their spectral characteristics. *European Journal of Soil Science* 63 1:42–53.

Chen, J., M. Yuan Zhang, L. Wang, H. Shimazaki, and M. Tamura. 2005. A new index for mapping lichen-dominated biological soil crusts in desert areas. *Remote Sensing of Environment* 96 (2):165–175.

Dettweiler-Robinson, E., Nuanez, M. & Litvak, M. E. (2018) Biocrust contribution to ecosystem carbon fluxes varies along an elevation gradient. Ecosphere, 9(6), e02315. Ferrenberg, S., C. L. Tucker, and S. C. Reed. 2017. Biological soil crusts: Diminutive communities of potential global importance. *Frontiers in Ecology and the Environment* 15 (3):160–167.

Garcia-Pichel, F., Belnap, J., 1996. Microenvironments and microscale productivity of cyanobacterial desert crusts. Journal of Phycology 32, 774–782.

Garcia-Pichel, F., Belnap, J., Neuer, S., Schanz, F., 2003. Estimates of global cyanobacterial biomass and its distribution. Algological Studies 109, 213–227.

Grote, E. E., Belnap, J., Housman, D. C. & Sparks, J. P. (2010) Carbon exchange in biological soil crust communities under differential temperatures and soil water contents: implications for global change. Global Change Biology, 16, 2763-2774.

Havrilla, C. A., M. L. Villarreal, J. L. DiBiase, M. C. Duniway, and N. N. Barger. 2020. Ultra-high-resolution mapping of biocrusts with unmanned aerial systems eds. N. Horning and J. Moat. *Remote Sensing in Ecology and Conservation*: rse 2.180.

Havstad K. M., Huenneke L. F., Schlesinger W. H. (2006). Chapter 3 / Climate and Climatological Variations in the Jornada Basin. In *Sturcture and Function of a Chihuahuan Desert Ecosystem: The Jornada Basin Long-Term Ecological Research Site* (pp. 46). Oxford University Press.

Herrick J. E., Zee J. W. V., McCord S. E., Courtright E. M., Karl J. W., Burkett L. M. (2018). In *Monitoring Manual for Grassland, Shrubland, and Savanna Ecosytems Second Edition: Volume I: Core Methods* (pp. 27). USDA-ARS Jornada Experimental Range.

Hoellrich M (2021). Biogeochemical function and microbial diversity in Chihuahuan desert biocrusts. *New Mexico State University Library*

Housman, D. C., Powers, H. H., Collins, A. D., & Belnap, J. (2006) Carbon and nitrogen fixation differ between successional stages of biological soil crusts in the Colorado Plateau and Chihuahuan Desert. Journal of Arid Environments, 66, 620-634.

Jensen JR 2007. Remote sensing of the environment: An earth resource perspective, 2nd edn. Pearson Prentice Hall, Upper Saddle River, NJ.

Karnieli, A., G. J. Kidron, C. Glaesser, and E. Ben-Dor. 1999. Spectral characteristics of cyanobacteria soil crust in semiarid environments. *Remote Sensing of Environment* 69 1:67–75.

Karnieli A 1997. Development and implementation of spectral crust index over dune sands. *Int. Journal of Remote Sensing Scimago* 18:1207–1220.

Karnieli A, V. Sarafis 1996. Reflectance spectrophotometry of cyanobacteria within soil crusts - A diagnostic tool. *Int. Journal of Remote Sensing Scimago* 17:1609–1614.

Kruse, F. A., Lefkoff, A. B., Boardman, J. W., Heidebrecht, K. B., Shapiro, A. T., Barloon, P. J., & Goetz, A. F. H. (1993). The Spectral Image Processing System (sips)—interactive visualization and analysis of Imaging Spectrometer Data. *Remote Sensing of Environment*, 44(2-3), 145–163. https://doi.org/10.1016/0034-4257(93)90013-n

Lange, O.L., 2003. Photosynthesis of soil-crust biota as dependent on environmental factors. In: Belnap, J., Lange, O.L. (Eds.), Biological Soil Crusts: Structure, Function, and Management, vol. 150. Springer, Berlin, pp. 217–240.

Li, M., S. Zang, B. Zhang, S. Li, and C. Wu. 2014. A review of remote sensing image classification techniques: The role of spatio-contextual information. *European Journal of Remote Sensing* 47 (1):389–411.

Maestre, F. T., J. L. Quero, N. J. Gotelli, A. Escudero, V. Ochoa, M. Delgado-Baquerizo, et al. 2012. *Plant species richness and ecosystem multifunctionality in global drylands*. Science 335 (6065), 214-218

Miralles, I., Ladrón de Guevara, M., Chamizo, S., Rodríguez-Caballero, E., Ortega, R., van Wesemael, B. & Cantón, Y. (2018) Soil CO2 exchange controlled by the interaction of biocrust successional stage and environmental variables in two semiarid ecosystems. Soil Biology and Biochemistry. 124, 11-23.

NOAA (2019) Comparative Climate Data: Mean number of days with precipitation 0.01 inch or more. https://www.ncdc.noaa.gov/data-access/quick-links#ccd

O'Neill, A. L. (1994). Reflectance spectra of microphytic soil crusts in semi-arid Australia. *International Journal of Remote Sensing*, 15(3), 675–681.

Petropoulos, G. P., Vadrevu, K. P., Xanthopoulos, G., Karantounias, G., & Scholze, M. (2010). A comparison of Spectral Angle Mapper and artificial neural network classifiers combined with Landsat TM imagery analysis for obtaining burnt area mapping. *Sensors*, *10*(3), 1967–1985. https://doi.org/10.3390/s100301967

Pietrasiak, N. (2012) Effects of land surface characteristics on pedogenesis, biological soil crust community diversity, and ecosystem functions in a Mojave Desert piedmont landscape. Ph.D. Dissertation. University of California, Riverside., U.S.A..

Pietrasiak, N., Regus, J. U., Johansen, J. R., Lam, D., Sachs, J. L., & Santiago, L. S. (2013). Biological soil crust community types differ in key ecological functions. *Soil Biology and Biochemistry*, 65, 168–171. https://doi.org/10.1016/j.soilbio.2013.05.011

Rodríguez-Caballero, E., P. Escribano, and Y. Cantón. 2014. Advanced image processing methods as a tool to map and quantify different types of biological soil crust. *ISPRS Journal of Photogrammetry and Remote Sensing* 90:59–67.

Rodríguez-Caballero, E., P. Escribano, C. Olehowski, S. Chamizo, J. Hill, Y. Cantón, and B. Weber. 2017. Transferability of multi- and hyperspectral optical biocrust indices. *ISPRS Journal of Photogrammetry and Remote Sensing* 126:94–107.

Rodríguez-Caballero, E., T. Knerr, and B. Weber. 2015. Importance of biocrusts in dryland monitoring using spectral indices. *Remote Sensing of Environment* 170:32–39.

Rozenstein, O., and J. Adamowski. 2017. A review of progress in identifying and characterizing biocrusts using proximal and remote sensing. *International Journal of Applied Earth Observation and Geoinformation* 57:245–255.

Saugier, B., Roy, J., Mooney, H.A., 2001. Estimates of global terrestrial productivity: converging toward a single number? In: Roy, J., Saugier, B., Mooney, H.A. (Eds.), Terrestrial Global Productivity. Academic Press, San Diego, pp. 543–557.

Shafri, H. Z., Suhaili, A., & Mansor, S. (2007). The performance of maximum likelihood, Spectral Angle Mapper, neural network and decision tree classifiers in hyperspectral image analysis. *Journal of Computer Science*, *3*(6), 419–423. https://doi.org/10.3844/jcssp.2007.419.423

Smith, W. K., M. P. Dannenberg, D. Yan, S. Herrmann, M. L. Barnes, G. A. Barron-Gafford, J. A. Biederman, S. Ferrenberg, A. M. Fox, A. Hudson, J. F. Knowles, N. MacBean, D. J. P. Moore, P. L. Nagler, S. C. Reed, W. A. Rutherford, R. L. Scott, X. Wang, and J. Yang. 2019.

SoilWeb. (2022). https://casoilresource.lawr.ucdavis.edu/gmap/USGS EarthExplorer. (2022). https://earthexplorer.usgs.gov/

Wadoux, J.-C., W. A. M., Malone, B. P., Minasny, B., Fajardo, M., & McBratney, A. B. (2022). Chapter 5 / Pre-processing of Spectra. In *Soil spectral inference with R: Analysing Digital Soil Spectra using the R Programming Environment* (pp. 52–53). essay, Springer.

Weber, B., C. Olehowski, T. Knerr, J. Hill, K. Deutschewitz, D. C. J. Wessels, B. Eitel, and B. Büdel. 2008. A new approach for mapping of biological soil crusts in semidesert areas with hyperspectral imagery. *Remote Sensing of Environment* 112 (5):2187–2201.

Wessels, D. C. J., & van Vuuren, D. R. J. (1986). Landsat imagery — its possible use in mapping the distribution of major lichen communities in the Namib Desert, South West Africa. *Madoqua*, 14(4), 369–373.

Young, K. E. 2016. Spectrally monitoring the response of the biocrust moss *Syntrichia caninervis* to altered precipitation regimes. *Scientific Reports* :10.

ProQuest Number: 31149373

INFORMATION TO ALL USERS

The quality and completeness of this reproduction is dependent on the quality and completeness of the copy made available to ProQuest.



Distributed by ProQuest LLC (2024). Copyright of the Dissertation is held by the Author unless otherwise noted.

This work may be used in accordance with the terms of the Creative Commons license or other rights statement, as indicated in the copyright statement or in the metadata associated with this work. Unless otherwise specified in the copyright statement or the metadata, all rights are reserved by the copyright holder.

This work is protected against unauthorized copying under Title 17, United States Code and other applicable copyright laws.

Microform Edition where available © ProQuest LLC. No reproduction or digitization of the Microform Edition is authorized without permission of ProQuest LLC.

ProQuest LLC 789 East Eisenhower Parkway P.O. Box 1346 Ann Arbor, MI 48106 - 1346 USA